JOURNAL OF AIRCRAFT
Vol. 40, No. 6, November–December 2003

Simulations of Mesoflap Control for Ramp-Generated Oblique Shock/Boundary-Layer Interactions

S. D. Kim,* E. Loth,† and J. C. Dutton‡
University of Illinois at Urbana–Champaign, Urbana, Illinois 61801

A novel flow-control method called mesoflaps for aeroelastic recirculation transpiration was computationally investigated for ramp-generated oblique shock/boundary-layer interactions (SBLIs). The numerical approach was first validated for three different ramp SBLI flows with a solid wall, in terms of both pressure distributions and velocity profiles. For the mesoflap flow-control method, a series of deflected flaps is placed over a cavity centered beneath the inception point of an oblique shock. The flow-control performance was investigated by measuring total pressure recovery and integral boundary-layer displacement thickness for a variety of preset flap deflection magnitudes and incoming Mach numbers. The control of an SBLI for a 16-deg compression corner with mesoflaps and incoming Mach numbers of 2.35–2.85 revealed significant improvement in total pressure recovery (as compared to the solid-wall case), especially as the deflections of the flaps increased. The lowest incoming Mach number investigated yielded the highest recovery of total pressure downstream of the shock. Although the flap cases yielded some increases in the displacement thickness and momentum thickness of the outgoing boundary layer as compared to the solid wall, the shape factor was maintained at approximately the same level as found for the solid-wall cases.

Introduction

IN a high-speed supersonic aircraft configuration, for example, $M_\infty = 2 \sim 5$, a forebody compression ramp produces an oblique shock to reduce the flow speed externally from the freestream value, followed by a normal shock near the inlet through which the flow becomes subsonic. The interaction of a ramp-generated oblique shock wave with a turbulent boundary layer yields large adverse pressure gradients, which, in turn, cause rapid thickening and possible separation of the boundary layer. The resulting shock/boundary-layer interaction (SBLI) may lead to stagnation pressure losses and distorted boundary-layer profiles that can seriously degrade engine performance. In general, the severity of the problem becomes greater as the flight speed of the aircraft increases. Similarly, ramp surfaces on other parts of the aircraft can yield significant drag penalties if the compression is far from isentropic. Therefore, it is of interest to study the effectiveness of flow-control systems for SBLIs in high-speed flows because efficient aerodynamic performance can minimize the total pressure losses and boundary-layer thicknesses and, thus, significantly improve the overall aircraft performance.

Although bleed flow can be used to effectively control the SBLI, it also results in drag and weight penalties that are roughly proportional to the magnitude of the bleed flow. As such, a flow-control technique that does not remove flow, while allowing good total pressure recovery, would be useful for such conditions.

Several previous studies have investigated recirculating flow-(passive-) control techniques as an alternative method of controlling SBLIs in high-speed flows.[1–5] Conventionally, the pressure rise caused by the shock imposes a pressure gradient on a porous surface, consisting of a series of slots or holes, covering a plenum chamber beneath the shock foot. This technique requires no external power source because the pressure gradient induces a natural recirculating flow resulting in both blowing upstream and bleed downstream of the shock. This transpiration can reduce the total pressure losses and wave drag, but is typically associated with a large increase in viscous drag. In addition, the performance of these conventional recirculating flow-control systems has been limited due to the additional viscous drag penalty incurred by the porous surface at no-shock or offdesign conditions.

A novel method of recirculating flow control has been designed to overcome these disadvantages. The aeroelastic mesoflap system consists of a matrix of flaps covering a plenum chamber (Fig. 1). The mesoflaps are designed to deflect aeroelastically in the presence of the shock due to the aerodynamic pressure load, resulting in recirculation of the flow similar to conventional passive control. The flap deflection may provide an aerodynamic advantage over conventional passive control by promoting upstream tangential injection and downstream tangential bleed. Also note that the deflection of the flaps will be larger as the shock pressure gradient increases, thereby automatically increasing the transpiration rate as is qualitatively desired. The mesoflaps can also allow high aerodynamic efficiency under subsonic flow conditions because the flap array acts as a nearly smooth flat plate when no shocks are present. The performance of the mesoflap system has been studied experimentally and computationally at the University of Illinois at Urbana–Champaign in the context of incident impinging oblique and normal SBLIs on a flat plate.[2,3] However, the present work is the first to investigate the capability of the mesoflaps to control ramp-generated oblique SBLIs for supersonic compression corners.

Numerical Method

The present two-dimensional computational analysis of compression corner flows generating an oblique shock wave was achieved using the FLUENT code together with the GAMBIT mesh generator. The numerical method is based on a control-volume technique that integrates the governing equations on hybrid structured–unstructured grids with a second-order upwind implicit scheme for the convection terms of the conservation equations. The flow was modeled with the Reynolds-averaged Navier–Stokes equations for a thermally and calorically perfect gas, employing the Boussinesq hypothesis for turbulence modeling. The two-layer k–ε turbulence model was selected to close the Reynolds-averaged conservation

Presented as Paper 2002-3117 at the AIAA 32nd Fluid Dynamic Conference and Exhibit, St. Louis, Missouri, 26 June 2002; received 17 January 2003; revision received 21 April 2003; accepted for publication 29 April 2003.

*Postdoctoral Research Associate, Department of Aeronautical and Astronautical Engineering, 306 Talbot Laboratory, 104 South Wright Street; sangkim3@uiuc.edu.

†Professor, Department of Aeronautical and Astronautical Engineering. Associate Fellow AIAA.

‡Professor, Department of Mechanical and Industrial Engineering. Associate Fellow AIAA.

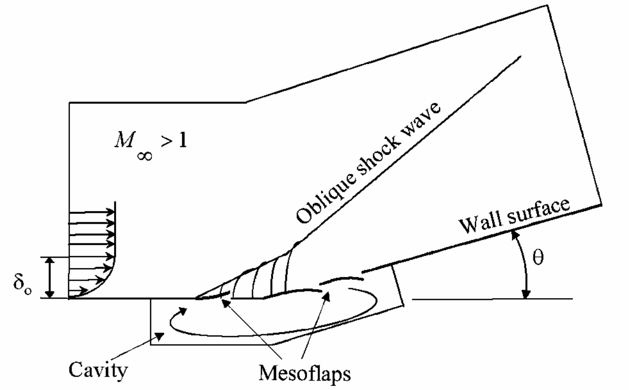

Fig. 1 Schematic diagram of a supersonic compression corner with mesoflaps.

equations because of its superior performance and stability as compared to other turbulence models for these ramp-compression flows.[6] The details of the conservation equations and the two-layer k–ε turbulence model are well documented in the literature.[7,8]

To obtain solutions to the conservation equations, proper boundary conditions are needed for the computational domain shown in Fig. 1. At the inflow boundary of the compression corner, for a supersonic freestream Mach number, the incoming flow properties were prescribed by the profiles obtained from the solution of a flat plate turbulent boundary-layer flow. At the compression corner, the flow is turned by angle θ. At the outflow boundary where the oblique shock exited the computational domain, the flow is mostly supersonic except for a small region next to the wall, so that all flow variables were extrapolated. The no-slip boundary condition and adiabatic wall condition were imposed on the wall surfaces. In the two-equation turbulence model, the turbulent kinetic energy and the dissipation rate were set to zero at the wall.

The grid system is composed of a structured boundary-layer mesh in the near-wall region and an unstructured mesh in the outer region. The structured viscous mesh employed a first-gridpoint placement from the wall at y^+ less than unity. A stretching function was used to cluster gridpoints near the wall and the oblique shock. Once the normal wall distance exceeded twice the boundary-layer thickness, the unstructured grid region was constructed for the rest of the domain. To provide high resolution near shocks, the grids were adapted based on density gradients. Typically, around 25,000 nodes were used for the initial mesh, and each mesh refinement (4 levels) increased the total number of nodes by about 10% such that the adapted mesh employed about 40,000 points. Convergence of the solutions was considered to be achieved when the L^2 norm of the maximum residual reached 10^{-4}.

Validation for Solid-Wall Compression Corners

The computed results for validation of the numerical scheme and the turbulence model are for solid-wall compression corner with $\theta = 8$, 12, and 16 deg. The freestream Mach number M_∞ was 2.94 and the incoming boundary-layer thickness δ_0 was 8.7 mm for the 8- and 12-deg compression corners. For the 16-deg ramp, M_∞ and δ_0 were 2.85 and 25 mm, respectively. The experimental data of Kuntz et al.[9] (for the 8- and 12-deg ramps) and Settles et al.[10] (for the 16-deg ramp) were compared with the current numerical results for evaluation of prediction fidelity. Figure 2 shows the surface pressure distributions along the wall for all three validation cases considered. The surface pressure is identical to the approach freestream value until the oblique shock occurs slightly upstream of the ramp, where the pressure increases rapidly. The pressure gradient then decreases downstream of the corner. The predicted pressures eventually reach a level close to the theoretical inviscid pressure rise far downstream of the shock, as expected.[11]

Comparisons of the velocity profiles at several locations along the surface for the 8-deg compression corner are shown in Fig. 3. The distance x^* from the shock location was nondimensionalized by the

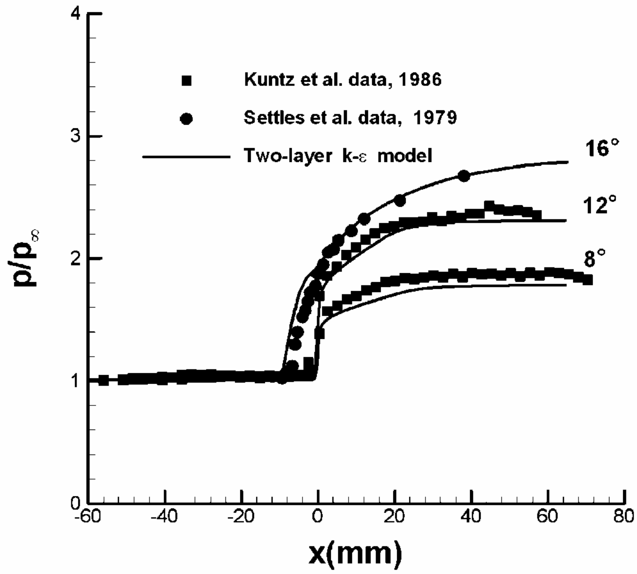

Fig. 2 Wall pressure distribution showing comparison of the two-layer k–ε prediction with the experimental data of Kuntz et al.[9] for 8- and 12-deg ramps and with the experimental data of Settles et al.[10] for a 16-deg ramp.

incoming boundary-layer thickness. The incoming boundary-layer velocity distribution is a fully developed turbulent profile (Fig. 3a), and as a result of the SBLI, the boundary layer is clearly seen to thicken. The prediction fidelity is especially good at the measurement locations far downstream of the shock ($x^* = 14 \sim 25$). For the stronger SBLI at 16-deg (Fig. 4), the experimental data were available only much closer to the shock location ($x^* = 0 \sim 1.5$). Although the current computational results show that the redevelopment of the boundary layer near the wall is somewhat slower downstream of the SBLI than is indicated by the experimental data, the computed results are generally consistent with the measurements in the region of this strong SBLI (with an especially good qualitative description of the boundary-layer shape in Figs. 4a and 4b). Based on Figs. 2–4, the computed results are largely in agreement with the pressure and velocity experimental data both upstream and downstream of the interaction for these solid-wall validation cases. This level of predictive fidelity was considered sufficient to have confidence in computationally evaluating the effect of mesoflap flow control on this type of SBLI.

Methodology for Mesoflap Simulations

The present computational analysis is the first study of a ramp-generated oblique SBLI with mesoflap control. As shown in Fig. 1, the ramp geometry and computational domain resemble the configuration of a supersonic forebody compression. All of the mesoflap cases were for a $\theta = 16$ deg compression corner and for inflow Mach numbers of 2.35, 2.6, and 2.85, which were selected to be similar to that of external precompression ramps of high-speed aircraft. In all cases, a cavity covered by three flaps was placed under the oblique shock where the first flap was deflected upward and the remaining two flaps were deflected downward. As such, all of the arrays studied herein consist of one injection flap (upstream) and two bleeding flaps (downstream). These three-flap arrays were chosen (as compared to four-, five-, or six-flap arrays) because they gave the best performance in terms of total pressure recovery and boundary-layer thickness in a preliminary study.[6] Note that the flap deflections were fixed and that their magnitudes were selected based on a priori aeroelastic estimates, but were not varied according to actual cavity pressure differences. Table 1 contains further details of the flow conditions and mesoflap array geometries that were studied herein.

Based on our previous study,[6] one of the most important parameters for SBLI control effectiveness is the flap deflection magnitude and is easily varied in these fixed-deflection computations. Detailed

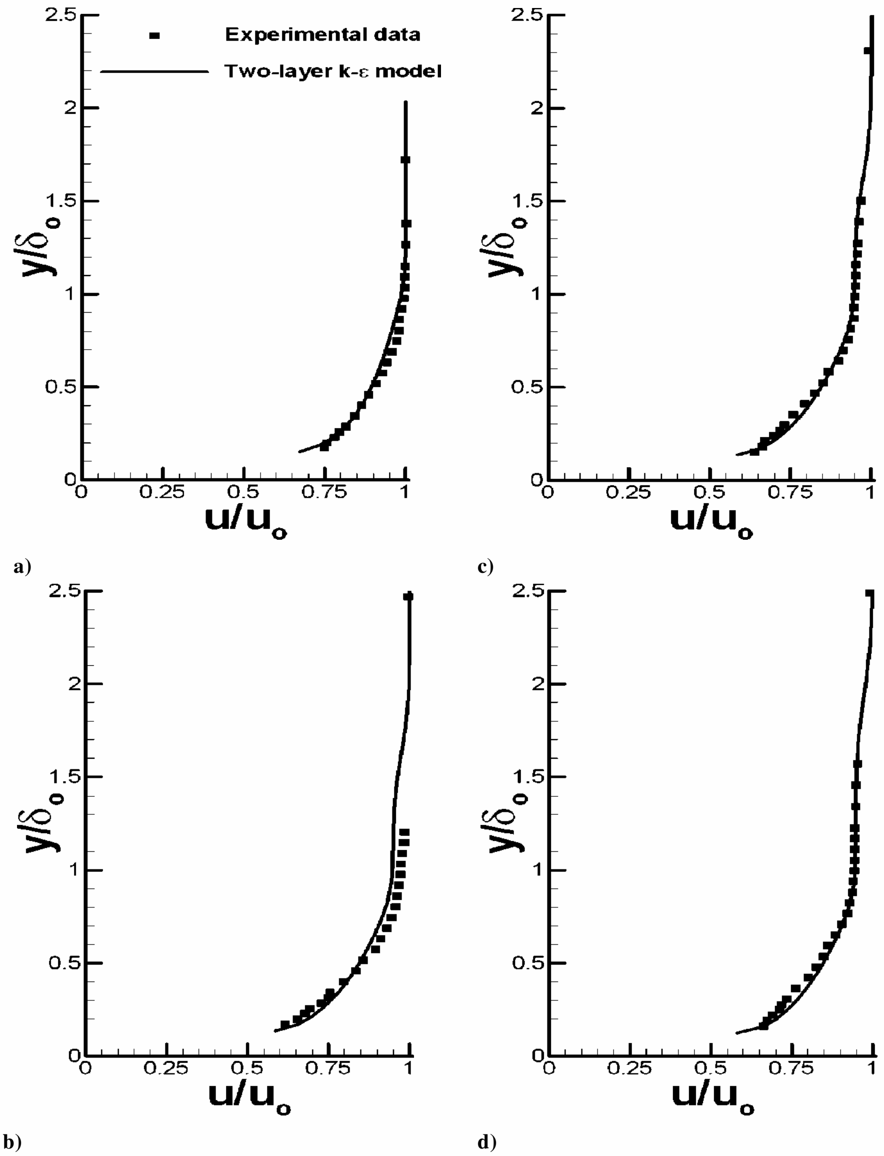

Fig. 3 Predicted mean velocity profiles compared with the experimental data of Kuntz et al.[9] for 8-deg ramp where a) $x^* = -2.8$, b) $x^* = 14$, c) $x^* = 19.5$, and d) $x^* = 25$.

Table 1 Flow conditions, geometry, and spacing of mesoflaps

Parameter	Value
Incoming Mach number	2.35, 2.6, 2.85
Reynolds number per meter	6.3×10^7
δ_0, mm	25
δ_0^*, mm	6
Flap length, $/\delta_0$	5
Flap thickness, $/\delta_0^*$	0.1
Spacing between upstream flap tip and shock, $/\delta_0$	5
Spacing between downstream flap tip and shock, $/\delta_0$	8

results will be presented with various flap deflections of such three-flap arrays for three different incoming Mach numbers, $M_\infty = 2.35$, 2.6, and 2.85. The upstream flap deflection was designated as $D1$, whereas the downstream flap deflections were set at $D2$, where both $D1$ and $D2$ are nondimensionalized by the incoming displacement thickness of the boundary layer δ_0^*. The cases chosen to investigate the dependence on deflection were initially designed for the deflection magnitudes to be on the order of the incoming boundary-layer displacement thickness. However, as will be shown, the total pressure recovery was not maximized until the flap deflections were significantly larger than δ_0^* for the current ramp-generated oblique shocks, such that the upstream flap deflections examined herein were varied from $0.3\delta_0^*$ to $3.0\delta_0^*$.

Also note that certain combinations of flap deflections gave results that would not be consistent with aeroelastic deflections, that is, generated by pressure difference across the flaps. For example, some combinations with high fixed bleed-flap deflections, for example $D2 > 0.4$ for $D1 = 1.2$ and $M_\infty = 2.85$ led to cavity pressures that exceeded the downstream static pressure above the wall. This effect, which was attributed to recovering much of the dynamic pressure of the freestream fluid bled into the cavity when reducing the flow speed, yielded a static pressure difference between the cavity and the flow above which would be inconsistent with a downward aeroelastic deflection of the bleed flaps.

A useful parameter describing total pressure recovery improvement downstream of the shock is defined as the pressure recovery index, that is,

$$\beta = \frac{\overline{p_t} - \overline{p_{t|\mathrm{sw}}}}{p_0 - \overline{p_{t|\mathrm{sw}}}} \tag{1}$$

where $\overline{p_t}$ is the mass-averaged total pressure for a controlled case with mesoflaps. This quantity was determined by integration from the wall to the oblique shock intersection point in the normal

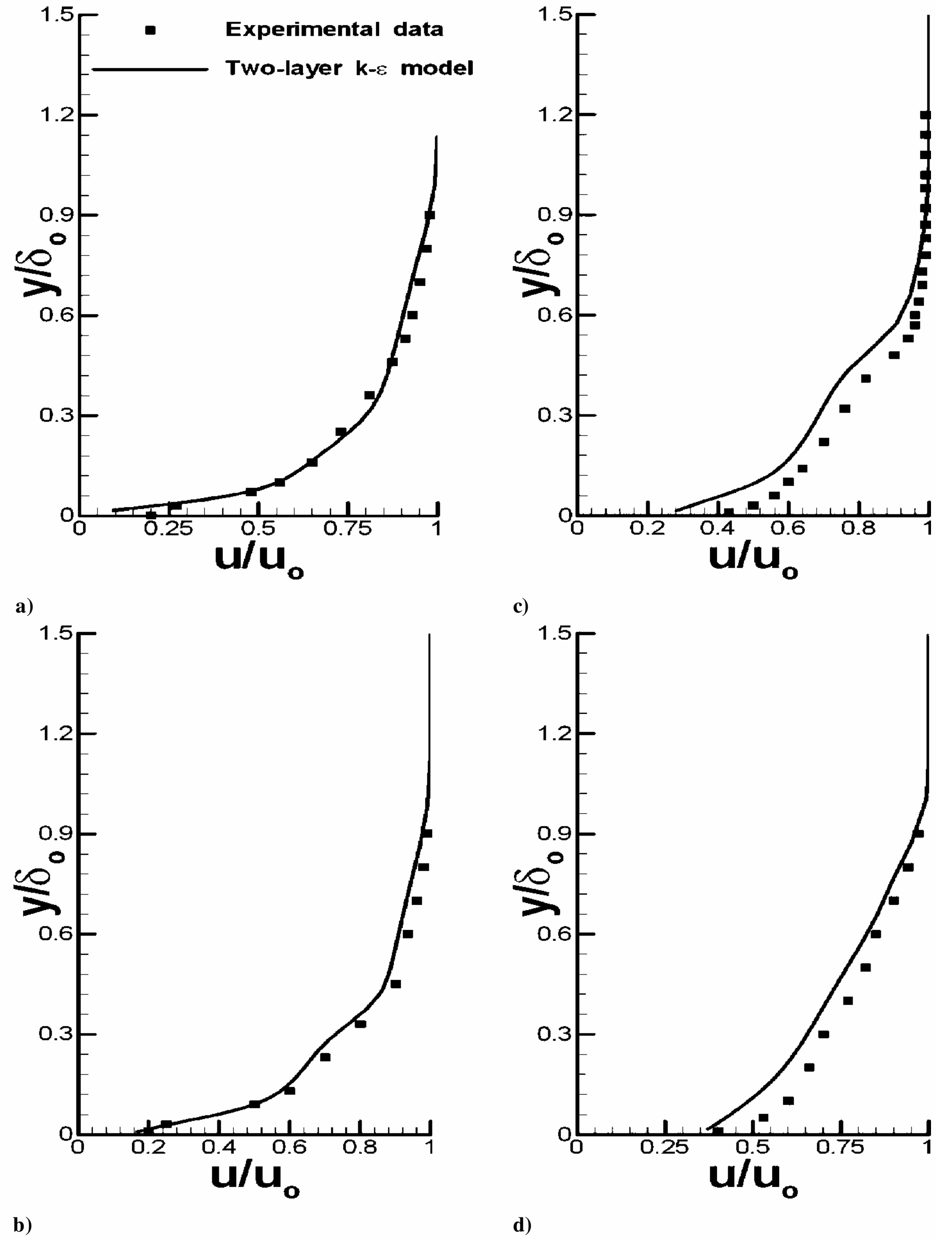

Fig. 4 Predicted mean velocity profiles compared with the experimental data of Settles et al.[10] for 16-deg ramp where a) $x^* = 0.0$, b) $x^* = 0.25$, c) $x^* = 0.75$, and d) $x^* = 1.5$.

direction,

$$\overline{p_t} = \int_{\ell=0}^{s} p_t \rho \boldsymbol{v} \cdot \boldsymbol{n} \, \mathrm{d}\ell \tag{2}$$

In the definition of β in Eq. (1), $\overline{p_{t|\mathrm{sw}}}$ is the mass-averaged total pressure for the solid-wall case, and p_0 is the inflow total pressure. The total pressure recovery improvement index β will be unity only for the isentropic compression of the flow and will equal zero for solid-wall recovery. The value of β will be positive only when the controlled case yields a higher total pressure recovery than for the solid-wall case. A related performance parameter is the mass-averaged total pressure recovery nondimensionalized by the inflow total pressure and is called the total pressure recovery parameter α,

$$\alpha = \overline{p_t}/p_0 \tag{3}$$

$$\Delta\alpha = \alpha - \alpha_{\mathrm{sw}} \tag{4}$$

where $\Delta\alpha$ is the difference of the total pressure recovery parameter α between the controlled case and the solid-wall case.

Figure 5 shows the computational grid for a typical mesoflap case that has the same general configuration as for the solid-wall case. The grid system consists of a structured boundary-layer mesh in the near-wall region and an unstructured mesh in the outer region. The unstructured grid was specially constructed in the vicinity of the flap tips (Figs. 5b and 5c), to provide high spatial resolution in these resigns. A stretching function was used to resolve the high transverse flow gradients near the wall. Note that grid adaptation, based on the density gradient, was used to resolve the oblique shock as in the case of the solid-wall simulations.

Figure 6 shows the grid dependence of the total pressure recovery improvement index β at $x^* = 55$ for the three-flap cases for which $D1/D2 = 0.9/0.3$. In this grid-resolution study, the number of grid points N was increased by further grid adaption and by inserting additional grid points on the boundaries, where N_0 is the baseline number of grid points, set as 37,000. The results indicate that the baseline number of grid points, N_0, used in the current study was sufficient to resolve the SBLI and to quantify the performance of the mesoflaps in terms of β because little change was noted for a near doubling of the number of grid points in the vicinity of this value.

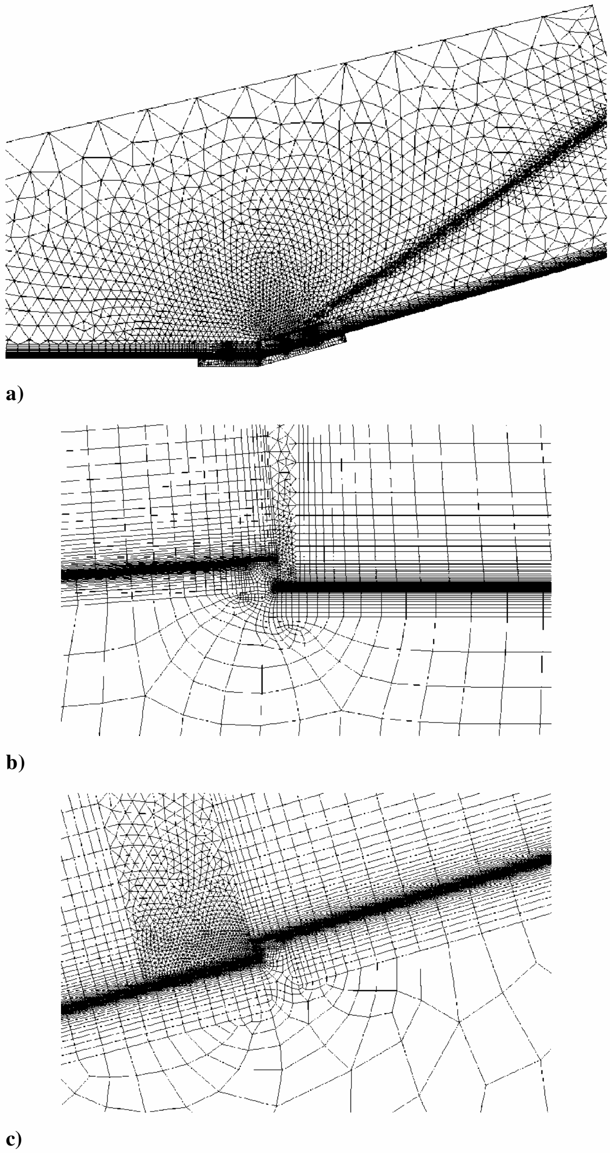

Fig. 5 Grid system for the 16-deg ramp with three flaps: a) overall grid system, b) near an injection gap, and c) a bleeding gap.

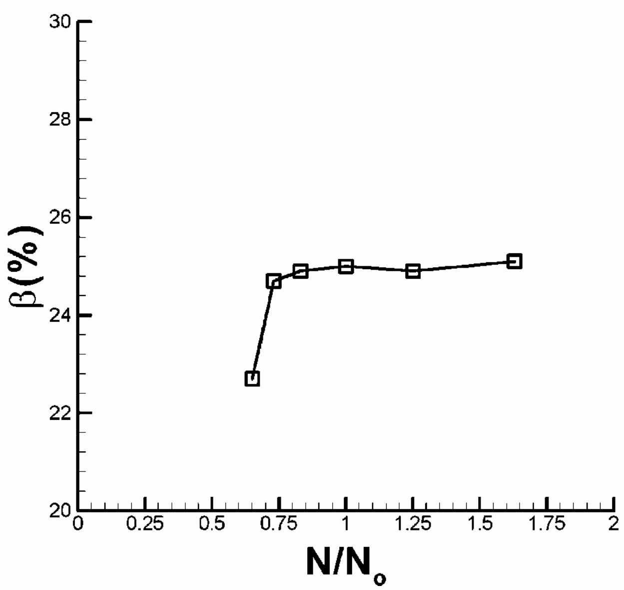

Fig. 6 Dependence of total pressure recovery index on number of grid points, where N_0 is the baseline value of 37,000 points.

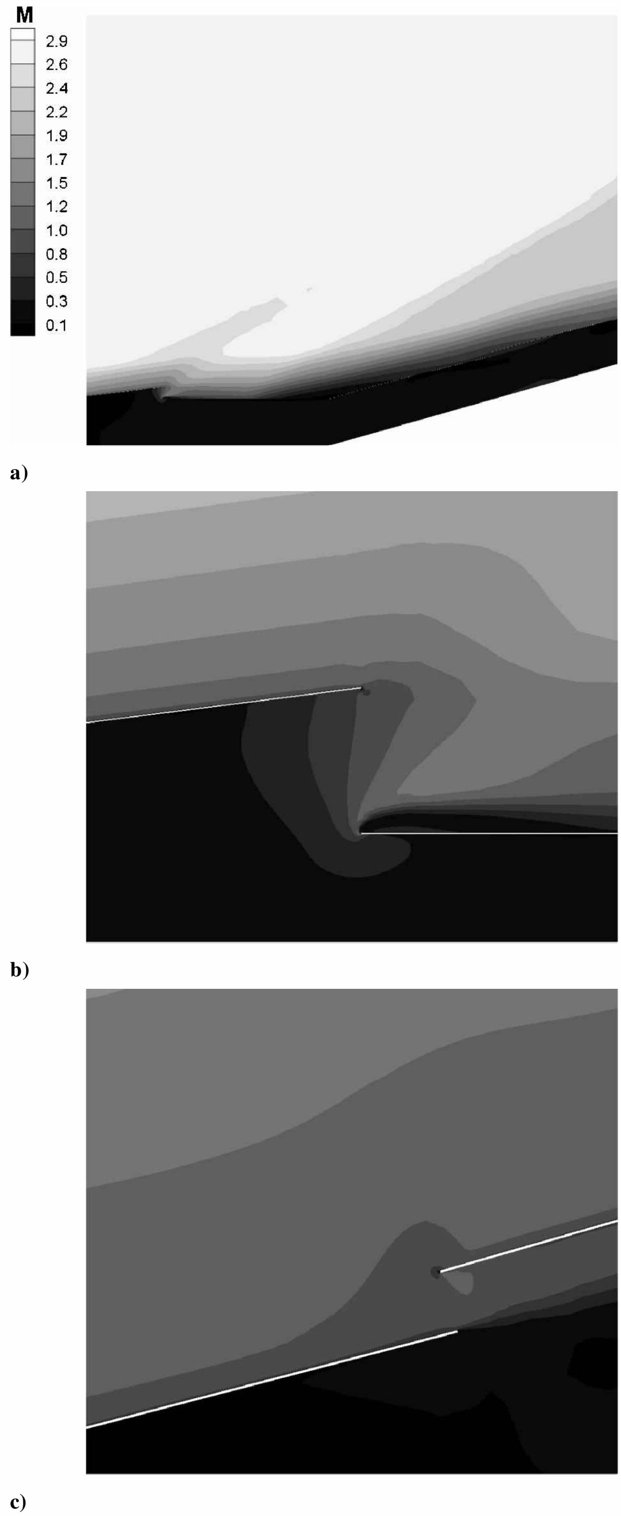

Fig. 7 Mach number contours over the 16-deg ramp with three flaps for $D1/D2 = 1.5/0.5$ and $M_\infty = 2.85$: a) overall flowfield, b) near an injection gap, and c) near a bleeding gap.

Results

The growth of the boundary layer through the SBLI for a typical mesoflap case can be seen in the Mach number contour plots of Fig. 7 for the 16-deg ramp with $D1/D2 = 1.5/0.5$ and $M_\infty = 2.85$. A fully turbulent boundary layer develops upstream of the shock until the upstream flap is encountered. Weak compression waves result from the upward deflection of the upstream flap, which are seen to perturb the incoming boundary layer in Fig. 7b. The oblique shock occurs just upstream of the compression corner and is strong enough

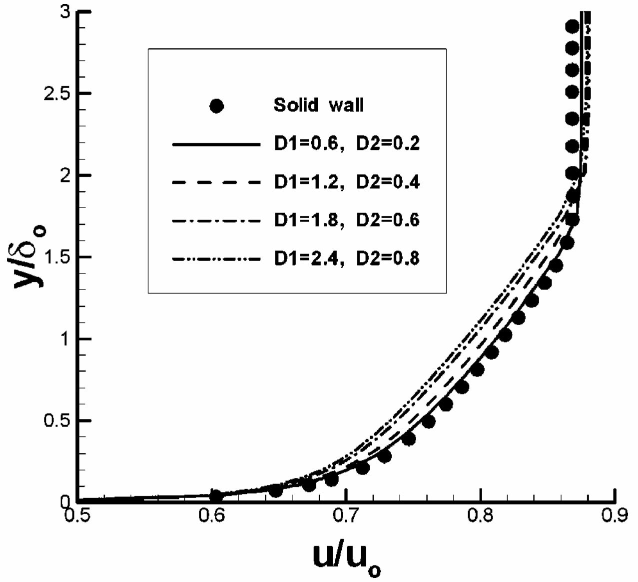

Fig. 8 Mean velocity profiles for various flap deflections at $x^* = 55$ for the 16-deg ramp and $M_\infty = 2.85$.

to cause boundary-layer separation downstream of the shock. In addition, expansion waves are caused by the downward deflection of the downstream flaps. Figure 7c shows that the low-momentum fluid near the wall is bled into the cavity through one of the bleeding gaps of the downstream flaps at about a Mach number of 0.5. The resulting downstream boundary-layer thickness is noticeably reduced. The bleed flow recirculates through the cavity at a very low Mach number and is tangentially injected into the outer flow through the gap of the upstream flap (Fig. 7b) at about a Mach number of 0.8. This tangential injection results in a moderate increase in boundary-layer thickness.

Figure 8 shows the outgoing mean velocity profiles at $x^* = 55$ and $M_\infty = 2.85$ for various flap deflections. In all cases, the $D1/D2$ ratio was kept as a constant to correspond to consistent changes in the thickness (or elasticity) of all of the flaps. The particular ratio employed, $D1/D2 = 3$, yielded the best performance, as will be discussed later. The near-wall velocity profiles of all flap cases are similar to the solid-wall reference case, but in general indicate a lower velocity at equivalent y/δ_0 locations. However, the velocity magnitude at the boundary-layer edge for the flap cases is slightly larger (due to a reduced overall shock strength) than for the solid-wall case. This change is associated with a nearly 15% increase in boundary-layer thickness over the solid-wall case for most of the mesoflap cases. In addition, the velocity profiles of the controlled cases recover from the SBLI more slowly within the boundary layer, resulting in an increased velocity defect near the wall as the flap deflection increases.

An important study of the effectiveness of the mesoflap system on the boundary-layer characteristics is a quantitative analysis of the boundary-layer integral properties. Figure 9a shows a comparison of the incompressible displacement thickness evolution for the various flap-deflection and solid-wall cases. The downstream displacement thickness of the solid-wall case is similar to its upstream value at $x^* = 10$ but then increases continuously as the boundary layer develops. In most of the flap cases, the displacement thickness at $x^* = 10$ is significantly larger than the upstream value especially as the flap deflection increases. Downstream of $x^* = 25$, the displacement thickness increases for the smaller flap deflections, although remaining nearly constant for the larger flap deflections. Similar trends are observed in the results for the incompressible momentum thickness evolution, as shown in Fig. 9b. In all cases, the momentum thickness increases downstream of $x^* = 25$ with increasing streamwise distance from the shock. Figure 9c shows the shape factor evolution for these cases, which is an indication of the health level of the boundary layer, in particular, its susceptibility to separation.

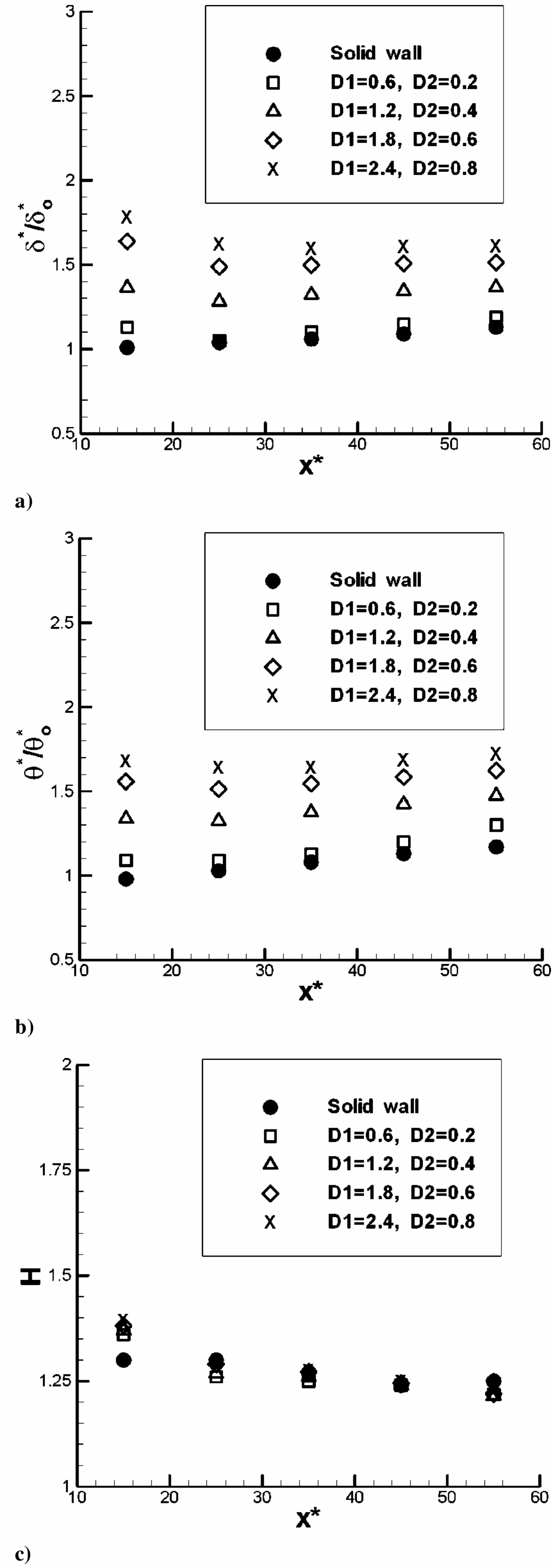

Fig. 9 Comparison of integral boundary layer parameters for $M_\infty = 2.85$: a) displacement thickness, b) momentum thickness, and c) shape factor.

In all cases, the shape factor shows a fully developed and healthy turbulent boundary layer that is far from separation for x^* of 10 or more because H is of the order of 1.25. The shape factor for all of the flap cases starts out slightly larger than for the solid-wall case at $x^* = 15$ because of the effect of the flow disturbance caused by the upward deflection of the upstream flap, but it decreases continuously to a value approximately 3% lower than for the solid-wall case. This indicates that the boundary-layer fullness is not adversely affected

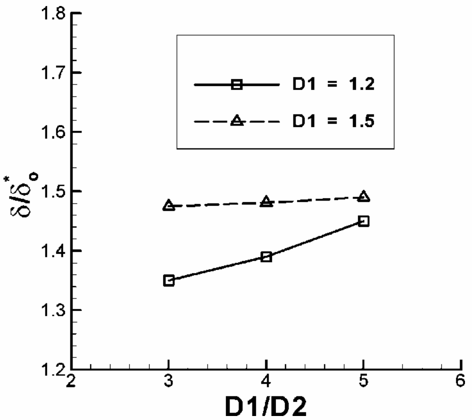

a)

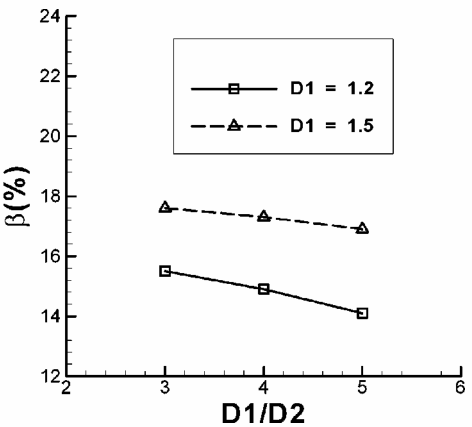

b)

Fig. 10 Performance parameters for different *D1/D2* ratios: a) displacement thickness and b) total pressure recovery index.

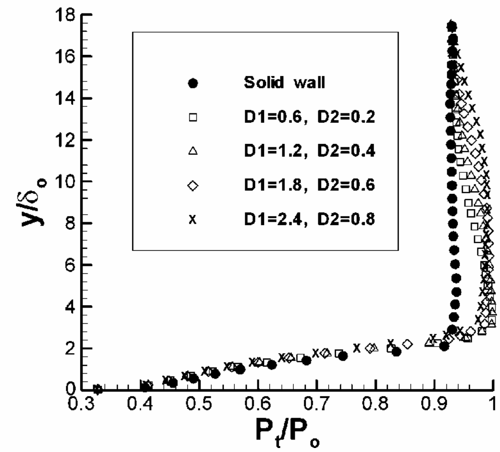

a)

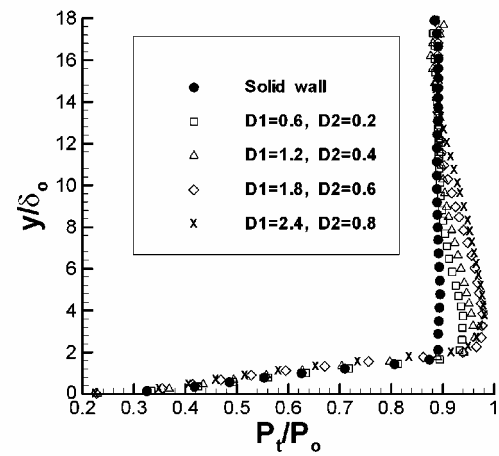

b)

Fig. 11 Total pressure profiles for various flap cases at $x^* = 55$: a) $M_\infty = 2.35$ and b) $M_\infty = 2.85$.

by the mesoflap deflections. This is important because improved total pressure recovery with conventional recirculating control (holes or slots) typically comes at the expense of boundary-layer health, with an associated increase in viscous losses.[3]

Figure 10 shows the effects of changing the flap deflection ratio $D1/D2$ (while maintaining $D1$ at two fixed values of 1.2 and 1.5) on the displacement thickness and total pressure recovery improvement index at $x^* = 55$ and $M_\infty = 2.85$. The smallest ratio of $D1/D2 = 3$ provides the best recovery of total pressure and the smallest increase of displacement thickness over the solid-wall case than does the largest ratio of $D1/D2 = 5$ (for both $D1 = 1.2$ and 1.5). This is particularly evident for the smaller upstream flap deflection ($D1 = 1.2$). One might expect that an even lower ratio of $D1/D2$ may further increase performance. However, when the ratio of $D1/D2 = 2$ was used (for both $D1 = 1.2$ and 1.5), the cavity pressure P_c exceeded the downstream static pressure in the outer flow, P_{down}. This occurred because the higher bleeding flap deflections captured more freestream momentum and, thus the cavity pressure approached the freestream stagnation pressure. This condition of $P_c > P_{\text{down}}$ is inconsistent with aeroelastic downward deflections for the downstream flaps and, thus, not generally considered. Therefore, the ratio $D1/D2 = 3$ was employed as the baseline value for further evaluation of the aeroelastic mesoflaps to be described.

Figures 11a and 11b show the total pressure profiles at $x^* = 55$ for the various flap deflections and the solid-wall reference case for $M_\infty = 2.35$ and 2.85. The total pressure recovery improvements of the flap cases are all in the region above the boundary layer and are significant when compared to the solid-wall case. These improvements are a result of a more gradual and, thus, nearly isentropic turning of the flow. This is due to a successively increased extent and strength of precompression waves associated with the upstream flap deflection. Note that the profiles are not severely distorted within the boundary layer even though the upstream flap deflection $D1$ was increased up to 2.4 for both freestream Mach numbers. The peak total pressure recovery is generally situated just above the boundary-layer edge, as was preliminarily indicated by the velocity profiles. This improvement feature is only seen for the mesoflap cases and indicates a more gradual turning of the flow just above the boundary-layer edge. It is notable that the peak pressure recovery at this point approaches unity (especially for the lower Mach number), indicating nearly isentropic compression locally. The improvement level and the peak total pressure tend to increase as the deflection of the flaps increases, except for the case of $D1/D2 = 2.4/0.8$ (the largest deflections) at $M_\infty = 2.35$. At this condition, it appears that the boundary-layer degradation caused by the upstream flap deflection has become substantial enough to impact negatively the precompression advantages to the total pressure peak. At the higher Mach number, $M_\infty = 2.85$, this degradation limit has not been reached for $D1/D2 = 2.4/0.8$, and this geometry yields an integrated total pressure recovery improvement index (up to the oblique shock intersection point) of 21.6% (Table 2). The boundary-layer resilience at these large flap deflections is attributed to the benefit of the precompression and the aerodynamic recirculation by the mesoflap system.

Three different Mach numbers (with the same boundary-layer thickness) were examined herein to find the effect of Mach number on the integrated total pressure recovery of the mesoflap-controlled cases (Fig. 12). The effectiveness of control of an oblique SBLI at lower Mach number (lower Reynolds number) is much more pronounced than at higher Mach number (higher Reynolds number). This is attributed to the larger vertical extent of the precompression turning, for example, in Fig. 11, improvements were seen up to $y/\delta_0 = 16$ for $M_\infty = 2.35$ but only up to $y/\delta_0 = 12$ for $M_\infty = 2.85$.

Table 2 Total pressure recovery indices, displacement thickness, and shape factor

$D1/D2$	$\Delta\alpha$, %	β, %	δ^*/δ_0^*	H
Mach number = 2.35				
Solid-wall case	0	0	1.8	1.3
0.3/0.1	0.3	2.5	2	1.287
0.6/0.2	2.0	15	2.1	1.28
0.9/0.3	2.4	19.2	2.2	1.273
1.2/0.4	3.0	21.7	2.3	1.275
1.5/0.5	3.4	25	2.4	1.276
1.8/0.6	3.63	26.7	2.5	1.28
2.4/0.8	3.5	25.9	2.67	1.29
3.0/1.0	3.4	25	2.8	1.31
Mach number = 2.85				
Solid-wall case	0	0	1.1	1.25
0.3/0.1	0.7	4	1.19	1.22
0.6/0.2	1.76	10.1	1.2	1.22
0.9/0.3	2.23	12.8	1.29	1.215
1.2/0.4	2.66	15.5	1.35	1.215
1.5/0.5	3.0	17.6	1.41	1.21
1.8/0.6	3.28	18.9	1.49	1.22
2.4/0.8	3.76	21.6	1.53	1.223
3.0/1.0	3.87	22.3	1.57	1.23

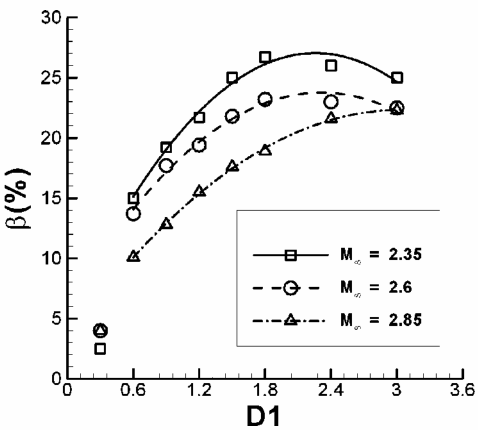

Fig. 12 Effect of upstream flap deflection, where $D2 = D1/3$ for all cases.

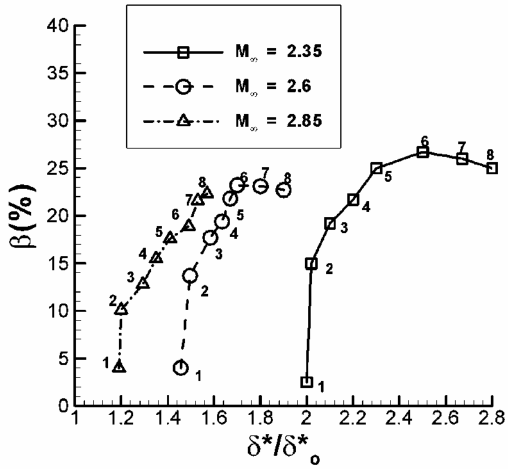

Fig. 13 Mach number effect on total pressure recovery index and displacement thickness where $D1/D2$ is given as 1, 0.3/0.1; 2, 0.6/0.2; 3, 0.9/0.3; 4, 1.2/0.4; 5, 1.5/0.5; 6, 1.8/0.6; 7, 2.4/0.8; and 8, 3.0/1.0.

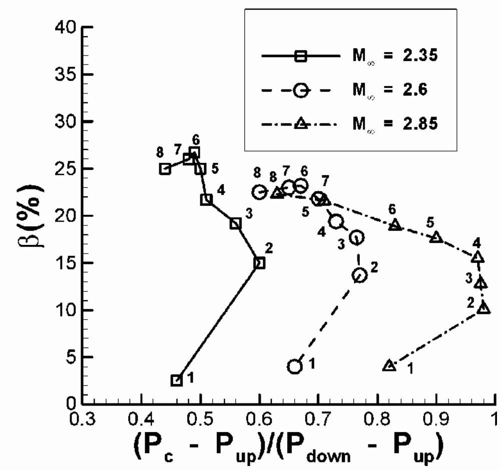

Fig. 14 Mach number effect on total pressure recovery index and cavity pressure where $D1/D2$ is given as 1, 0.3/0.1; 2, 0.6/0.2; 3, 0.9/0.3; 4, 1.2/0.4; 5, 1.5/0.5; 6, 1.8/0.6; 7, 2.4/0.8; and 8, 3.0/1.0.

The total pressure recovery improvement index increases with increasing flap deflection until the case of $D1/D2 = 1.8/0.6$ (which is a deflection greater than the sonic thickness) for the two lower Mach number cases. These improvements are based on the increased upstream flap deflection and boundary-layer bleed, which increases recirculation in the cavity substantially. In contrast to the two lower Mach numbers, the total pressure recovery index at a Mach number of 2.85 continuously increases with increasing flap deflection over the range investigated. This is attributed to a higher Mach number, as compared to the $M_\infty = 2.35$ and 2.6 cases, such that the impact of boundary-layer degradation is substantially reduced for $M_\infty = 2.85$.

To consider simultaneously the aspects of both pressure recovery and boundary-layer thickness, β and δ^* were evaluated for a variety of mesoflap deflections in Fig. 13. As the peak total pressure recovery index downstream of the shock increases, the displacement thickness also increases. The lowest Mach number case particularly yields a higher total pressure recovery at the expense of substantial boundary-layer thickening for $D1 > 1.8$. However, all of the Mach number cases for $D1 \leq 0.6$, that is, cases 1 and 2, indicated substantial improvements in pressure recovery with negligible increases in boundary-layer displacement thickness. Therefore, this may be considered an optimum condition if boundary-layer thickness is critical.

Finally, Fig. 14 shows the Mach number effect on the relation between the dimensionless cavity pressure and total pressure recovery index. P_c, $P_{\rm up}$, and $P_{\rm down}$ are the static pressure in the cavity chamber, upstream, and downstream of the shock, respectively. For flap deflections greater than $D1/D2 = 0.6/0.2$, the nondimensional cavity pressure for a given Mach number decreased as the flap deflection increased. This suggests that larger deflections of the upstream flap sufficiently degenerated the boundary-layer profiles before the bleeding locations to reduce consistently the velocity profile to be bled and, thus, also to reduce the amount of overall dynamic pressure recovered in the cavity chamber. Figure 14 also shows that, as the Mach number increased, higher static pressure recovery in the cavity occurred. In general, the good performance of the mesoflaps at $D1/D2 = 0.6/0.2$ noted in Fig. 13 is correlated with the high cavity static pressure recovery noted in Fig. 14. This suggests that ensuring good aerodynamic recovery of the incoming flow with tangential bleed is critical to overall system performance. In addition, maximizing the cavity pressure may be a reasonable way to optimize approximately, system performance because measurements of P_c are relatively simple (as opposed to relying on detailed investigation of total pressure and velocity profiles).

Conclusions

A computational investigation was conducted to study the potential capability of mesoflap arrays to control ramp-generated oblique SBLIs. A ratio of 3:1 for upstream to downstream deflection magnitude was found to be optimum and was used as the baseline case. The total pressure performance improvements of the flap cases are significant when compared to the solid-wall case, and the improvement level increased generally with increasing flap deflections until the deflections became excessive, for example, upstream deflections greater than twice the displacement thickness. Although the flap cases yield an increase in the outgoing boundary-layer displacement thickness and momentum thickness for a 16-deg oblique SBLI, the shape factor did not increase over the solid-wall case. This result indicates that boundary-layer characteristics are not seriously affected by the mesoflap control systems.

Moderate upstream flap deflections (about on the order of the displacement thickness) yielded substantial total pressure recovery performance for the 16-deg oblique SBLI with a negligible increase of downstream boundary-layer thickness. This precompression allowed a nearly isentropic recovery just above the boundary-layer edge, which is attributed to the upstream flap deflection. The nondimensional cavity pressure was found to be maximized at about this same optimum condition, indicating that efficient aerodynamic recovery was critical to overall SBLI improvements. However, the cavity pressure must be less than the static pressure downstream of the shock to allow aeroelastic behavior of the mesoflap control. The performance enhancements seen in the current numerical simulations indicate the potential capability of the mesoflap system to control oblique SBLIs in compression corners.

Acknowledgments

This work was supported under Contract F49620-98-1-0490 by the Defense Advanced Research Projects Agency with Rich Wlezien as Technical Monitor and the Air Force Office of Scientific Research with Steven Walker as Technical Monitor. This work is also supported by the Postdoctoral Fellowship Program of Korea Science and Engineering Foundation.

References

[1]Raghunathan, S., "Passive Control of Shock Boundary Layer Interaction," *Progress in Aerospace Science*, Vol. 25, No. 3, 1988, pp. 271–296.

[2]Gefroh, D. L., Loth, E., Dutton, J. C., and McIlwain, S., "Control of an Oblique Shock/Boundary-Layer Interaction with Aeroelastic Mesoflaps," *AIAA Journal*, Vol. 40, No. 12, 2002, pp. 2456–2466.

[3]Hafenrichter, E. S., Lee, Y., McIlwain, S. T., Dutton, J. C., and Loth, E., "Experiments on Normal Shock/Boundary Layer Interaction Control Using Aeroelastic Mesoflaps," AIAA Paper 2001-0156, Jan. 2001.

[4]Bur, R., Corbel, B., and Delery, J., "Study of Passive Control in a Transonic Shock-Wave/Boundary-Layer Interaction," *AIAA Journal*, Vol. 36, No. 3, 1998, pp. 394–400.

[5]McCormick, D. C., "Shock/Boundary-Layer Interaction Control with Vortex Generators and Passive Cavity," *AIAA Journal*, Vol. 31, No. 1, 1993, pp. 91–96.

[6]Kim, S. D., Loth, E., and Dutton, J. C., "Simulations of Mesoflap Flow Control for Ramp Oblique Shock/Boundary Layer Interactions," AIAA Paper 2002-3117, June 2002.

[7]Barth, T. J., and Jespersen, D., "The Design and Application of Upwind Schemes on Unstructured Meshes," AIAA Paper 89-0366, Jan. 1989.

[8]Chen, H. C., and Patel, V. C., "Near-Wall Turbulence Models for Complex Flows Including Separation," *AIAA Journal*, Vol. 26, No. 2, 1988, pp. 641–648.

[9]Kuntz, D. W., Amatucci, V. A., and Addy, A. L., "Turbulent Boundary-Layer Properties Downstream of the Shock Wave/Boundary-Layer Interaction," *AIAA Journal*, Vol. 25, No. 5, 1987, pp. 668–675.

[10]Settles, G. S., Fitzpatrick, T. J., and Bogdonoff, S. M., "Detailed Study of Attached and Separated Compression Corner Flowfields in High Reynolds Number Supersonic Flow," *AIAA Journal*, Vol. 17, No. 6, 1979, pp. 579–585.

[11]Erm, L. P., Smits, A. J., and Joubert, P. N., "Low Reynolds Number Turbulent Boundary Layers on a Smooth Flat Surface in a Zero Pressure Gradient," *Turbulent Shear Flow*, Spring-Verlag, Berlin, Heidelberg, Vol. 5, 1987, pp. 186–196.